ACCSCIENCE PUBLISHING

International Journal of Bioprinting

RESEARCH ARTICLE

3D-printed biomimetic liposomal hydrogels for localized and targeted treatment of drug-resistant *Candida albicans* vaginitis

Lina Dong[1†], Wenyan Wang[2†], Bixing Fang[3†], Meixuan Liu[1], Miao Pan[1], Xiaoqi Li[1], Aobuliaximu Yakupu[1], Chunmao Han[1], Qiong Li[1]*, and Xingang Wang[1]*

[1]Department of Burns and Wound Care Center, The Second Affiliated Hospital, Zhejiang University School of Medicine, Hangzhou, Zhejiang, China

[2]School of Pharmaceutical Sciences (Shenzhen), Sun Yat-sen University, Shenzhen, Guangdong, China

[3]Department of Otolaryngology, The Second Affiliated Hospital, Zhejiang University School of Medicine, Hangzhou, Zhejiang, China

Abstract

The excessive use of antibiotics has precipitated the emergence of drug-resistant bacterial strains, underscoring the critical need for developing novel, targeted antimicrobial agents. Among the burgeoning class of nanomaterials, silver clusters have attracted considerable attention due to their broad-spectrum and enduring antimicrobial properties, coupled with the crucial advantage of not eliciting resistance. These features render them exceptionally promising in the landscape of antimicrobial therapy. Nevertheless, the constraints associated with the topical application of silver clusters and the adverse effects linked to high-dose shock therapy pose significant challenges that require resolution. To surmount these obstacles, we engineered a sophisticated nanodrug delivery system capable of specific bacterial recognition and synergistic interaction with antimicrobial agents to accomplish precise antibacterial efficacy. Through the interaction between bacterial recognition receptor proteins (TLR2 and TLR4) on macrophage membranes and pathogen-specific molecular patterns on bacteria, we observed that cultivating macrophages in the presence of specific bacteria markedly upregulated the expression of these receptors. We subsequently isolated these specialized membrane proteins, integrated them into liposomes, and loaded silver clusters to formulate composite biomimetic liposomes (Lip@MOMP$_2$@AgNCs). These liposomes can be effectively administered to sites of vaginal infection via intravenous injection, facilitating specific bacterial recognition, and precise targeting. Moreover, we devised a 3D-printed hydrogel mesh scaffold incorporating Lip@MOMP$_2$@AgNCs, which amalgamates the injectable liposomal formulation with the 3D-printed hydrogel scaffold to realize sustained and localized drug release. This investigation not only advances a specific and promising therapeutic strategy for combating drug-resistant *Candida albicans* vaginitis but also forges new pathways in addressing the formidable challenge of antibiotic resistance.

Keywords: 3D printing; Hydrogel; Liposomes; Silver nanoclusters; Vaginitis

†These authors contributed equally to this work

***Corresponding authors:**
Qiong Li
(liqiongzessk@zju.edu.cn)

Xingang Wang
(wangxingang8157@zju.edu.cn)

Citation: Dong L, Wang W, Fang B, et al. 3D-printed biomimetic liposomal hydrogels for localized and targeted treatment of drug-resistant *Candida albicans* vaginitis. *Int J Bioprint*. 2025;11(1):485-500. doi: 10.36922/ijb.5851

Received: November 11, 2024
Revised: December 23, 2024
Accepted: January 3, 2025
Published Online: January 3, 2025

Copyright: © 2025 Author(s). This is an Open Access article distributed under the terms of the Creative Commons Attribution License, permitting distribution, and reproduction in any medium, provided the original work is properly cited.

Publisher's Note: AccScience Publishing remains neutral with regard to jurisdictional claims in published maps and institutional affiliations.

1. Introduction

Vulvovaginal candidiasis (VVC) represents a pervasive and complex clinical condition, afflicting approximately 75% of women with at least one episode during their lifetime, with 50% experiencing recurrent infections.[1] A striking 80% of these cases are ascribed to the most pathogenic species of *Candida*, notably *Candida albicans*.[2] The prevailing treatment modalities, which encompass the application of 2–3% sodium bicarbonate solutions for vaginal irrigation or sitz baths, frequently yield suboptimal outcomes, extending the therapeutic process and occasionally culminating in disease recurrence.

As delineated by the Centers for Disease Control and Prevention (CDC) guidelines established in 1998, the prescribed oral medication for recurrent VVC is fluconazole, administered at a dosage of 150 mg weekly over 6 months.[3,4] Nonetheless, this therapeutic regimen not only necessitates a protracted duration to attain efficacy but also falters in the complete eradication of hyphae and spores. Furthermore, the protracted use of fluconazole may foster resistance development in *C. albicans*.[5] Recent investigations have unveiled that 14.6% of *C. albicans* strains manifest significantly diminished sensitivity to fluconazole.[6] Thus, there exists a pressing imperative to devise an effective antimicrobial agent with a reduced propensity for resistance to treat resistant *Candida vaginitis*.

In this milieu, silver nanoparticles (AgNPs) have garnered substantial interest due to their exceptional antibacterial attributes, demonstrating considerable promise for clinical applications.[7–9] However, the nanoscale dimensions of silver nanoparticles elicit concerns regarding cytotoxicity to normal tissue cells, thereby constraining their clinical utility.[10–12] Overcoming the limitations of silver nanoparticles and alleviating the deleterious effects of systemic accumulation within the body emerge as critical challenges.

To this end, we propose the development of an efficacious drug delivery system exhibiting outstanding biocompatibility. To mitigate the cytotoxic repercussions of silver nanoparticles on human tissues, we have opted for glutathione-modified silver nanoclusters (AgNCs) as our antimicrobial agents. These nanoclusters, characterized by their diminutive size,[13] enable effective renal clearance and manifest substantial activity against resistant strains while upholding commendable biocompatibility.[14] To further diminish direct contact between AgNCs and normal tissues and to prolong the duration of drug release *in vivo*, we encapsulated AgNCs within liposomes.

Moreover, inspired by the pioneering research of Wang et al.[15] on the precise treatment of bacterial infections, we adorned the liposomes with specific receptor proteins extracted from pretreated macrophage membranes. TLR2 and TLR4, located on bacterial membranes, play a pivotal role in recognizing bacterial membrane components,[16,17] thereby endowing the liposomes with the capability to specifically target bacteria.

To achieve sustained and localized drug delivery, we integrated injectable liposomal formulations with 3D-printed hydrogel scaffolds. Recent advances in 3D bioprinting technology have demonstrated its potential for the precise fabrication of hydrogel scaffolds with tailored structural and mechanical properties.[18–20] Various bioprinting techniques, including extrusion-based, jetting-based,[21] and vat photopolymerization-based methods,[22] have been developed for hydrogel deposition, each with unique advantages and limitations. Extrusion-based bioprinting, widely recognized for its compatibility with high-viscosity bioinks and ability to create complex structures,[23] was selected for this study due to its superior printability and ease of use in fabricating stable hydrogel scaffolds suitable for drug delivery applications. This approach ensures precise deposition and structural integrity while accommodating the rheological properties of the hydrogel precursors.

In conclusion, we have engineered a biomimetic liposome system constructed from a phospholipid bilayer, incorporating specific membrane proteins from macrophages to facilitate selective bacterial recognition, and loaded with AgNCs to achieve precise and effective treatment of resistant *C. albicans* infections. Furthermore, the incorporation of extrusion-based 3D bioprinting technology into our platform enhances the controlled release and localized delivery of the therapeutic agents (Scheme 1), offering a more effective treatment option for clinical application.

2. Materials and methods

2.1. Materials

Hyaluronic acid (HA; molecular weight 100–200 kDa) was acquired from Lifecore Biomedical (United States of America [USA]). Methacrylic anhydride (MA), Irgacure 2959, Carbomer 940, and phospholipids (i.e., dipalmitoylphosphatidylcholine [DPPC], distearoylphosphatidylcholine [DSPC], and dioleoylphosphatidylcholine [DOPC]), were procured from Sigma–Aldrich (USA). Cholesterol and estradiol benzoate were sourced from Macklin (China). Monoclonal antibodies, that is, CD282 (TLR2), CD284 (TLR4), and

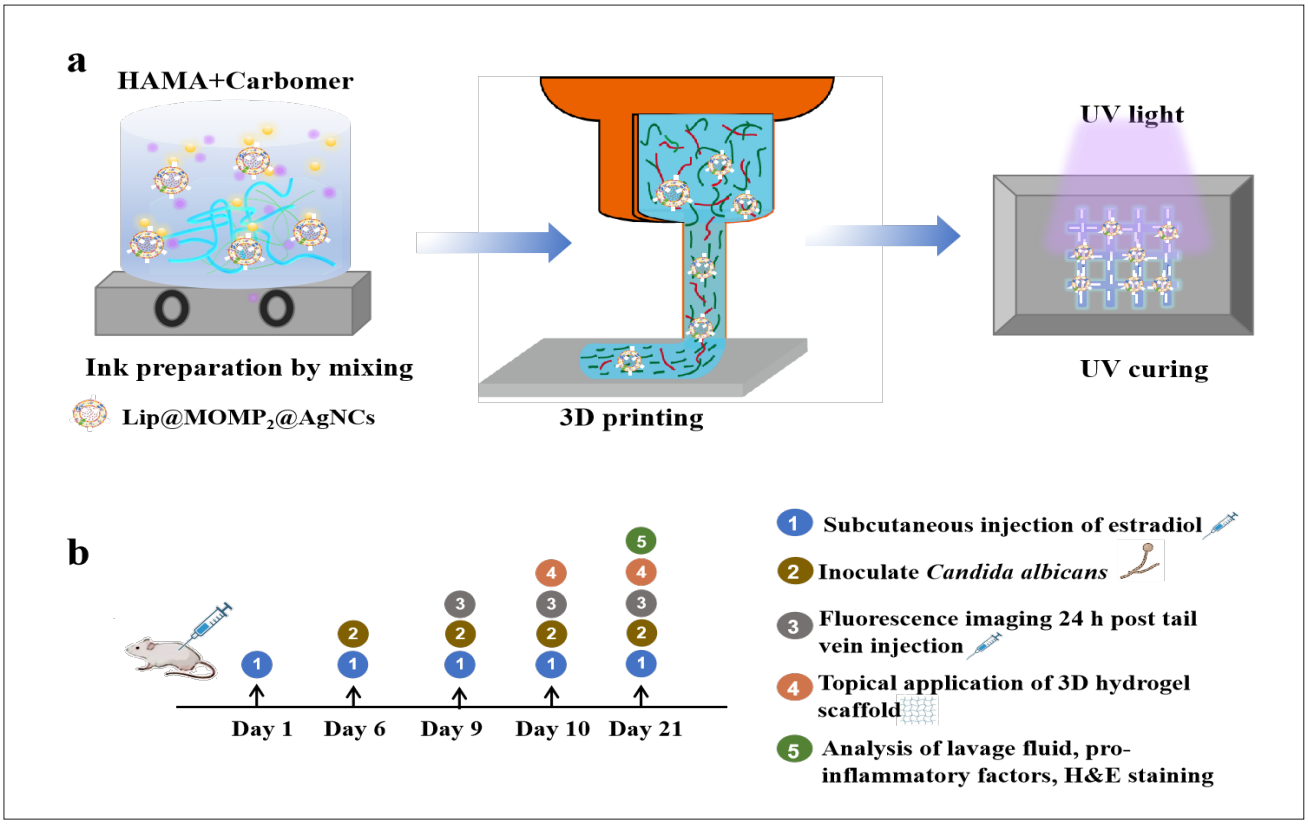

Scheme 1. Preparation and application of Lip@MOMP$_2$@AgNCs hydrogel *in vivo study.* (a) Lip@MOMP$_2$@AgNCs hydrogel printing process. (b) Animal study process, illustrating the administration of the hydrogel formulation *in vivo* in a mouse model. Abbreviations: HAMA, hyaluronic acid; H&E, Hematoxylin and Eosin Staining; UV, ultraviolet.

CD45, were obtained from Thermo Fisher Scientific (USA). Fourier transform infrared spectroscopy (FT-IR, Nicolet iS50, USA) was employed to analyze the lyophilized hydrogel samples within the spectral range of 4000–400 cm^{-1}. The AgNCs particle size distribution of the samples was measured using a Zetasizer Nano-ZS, which can detect sizes from 0.3 to 10,000 nm.

2.2. Preparation of AgNCs

In accordance with the methodology[14] previously delineated by our research group, aqueous solutions of $AgNO_3$ (1.25 mL, 20 mM) and glutathione (GSH; 1.5 mL, 50 mM) were initially amalgamated in 50 mL of distilled water. Under vigorous agitation, 0.5 mL of a $NaBH_4$ (112 mM) solution was introduced to the mixture. Within 5 min, a wine-red solution materialized, which was subsequently allowed to incubate at ambient temperature for 3 h, transitioning to a colorless state. Thereafter, an additional 0.5 mL of the $NaBH_4$ solution was incrementally added, followed by intensive stirring for 30 min and an aging period of 6 h, culminating in the formation of a red AgNCs solution. The synthesized AgNCs were then subjected to purification via ultrafiltration (3000 Da) and stored at 4 °C for subsequent utilization.

2.3. Extraction of macrophage membrane proteins MOMP$_1$ and MOMP$_2$

Macrophage membrane proteins were meticulously extracted using a membrane protein extraction kit from untreated J774.A1 cells, resulting in the isolation of MOMP$_1$ post-purification. In parallel, MOMP$_2$ was obtained from the membrane proteins of J774.A1 cells that had been exposed to *C. albicans*. The concentrations of these proteins were quantitatively measured using a BCA protein assay kit. Subsequently, equivalent amounts of both membrane proteins were subjected to Western blot analysis to evaluate the expression levels of TLR2, TLR4, and CD45.

2.4. Synthesis of Lip@MOMP$_2$

Lip@MOMP$_2$ was synthesized through the thin-film dispersion technique. A concoction of DPPC, DSPC, DOPC, and cholesterol was dissolved in a chloroform–methanol solution (3:1 v/v) at a precise molar ratio of

5:1:3:1. The solvent was meticulously removed using a rotary evaporator, thus creating a thin lipid film. $MOMP_2$, with a membrane protein to lipid weight ratio of 1:300, was subsequently dispersed in phosphate-buffered saline (PBS). This mixture was subjected to three cycles of vigorous vortexing at 45 °C, each lasting 3 min, to ensure proper hydration of the lipid film. The resultant Lip@$MOMP_2$ suspension was then extruded 10 times through a cellulose acetate membrane with a 200 nm pore size at 45 °C to obtain unilamellar vesicles. Finally, these vesicles were dialyzed overnight using a 1000 kDa membrane to effectively remove any residual solvents and unbound $MOMP_2$.

2.5. Assembly of Lip@$MOMP_2$@AgNCs

Lip@$MOMP_2$, AgNCs (50 μg/mL), and 2% $NaHCO_3$ were mixed in a ratio of 2:1:2 and incubated at 45 °C for 30 min. The mixture was then dialyzed for 3 h using a 1000 kDa membrane to obtain Lip@$MOMP_2$@AgNCs.

2.6. Release kinetics of Lip@$MOMP_2$@AgNCs

Drug release experiments were meticulously conducted using 200 mL of PBS (pH 4.2) and vaginal simulation fluid (pH 6.8) as the release media, both maintained at a constant temperature of 37 °C with continuous agitation at 60 rpm. The release of the encapsulated Lip@$MOMP_2$@AgNCs was monitored over a defined temporal course. At predetermined intervals—specifically 10, 20, 30, 60 min, 1, 1.5, 2, 3, 4, 5, 6, 9, 12, 18, and 24 h—1 mL aliquots of the release medium were carefully withdrawn and immediately replenished with an equivalent volume of fresh medium to maintain equilibrium. The ultraviolet (UV) absorbance of the aliquots was measured, facilitating the calculation of drug concentration via a standard curve.

2.7. Synthesis of the Lip@$MOMP_2$@AgNCs hydrogel

Hyaluronic acid methacrylate (HAMA) was synthesized in accordance with a previously established protocol.[24] Following this, 2% carbopol was incorporated into the HAMA solution in varying mass ratios of HAMA to Carbopol, specifically 1:2, 3:2, and 5:2, yielding distinct hydrogel precursors. To these mixtures, Lip@$MOMP_2$@AgNCs were introduced at varying concentrations—250, 500, 750, and 1000 μg/mL—and were meticulously dispersed throughout the HAMA-carbopol solutions. This process resulted in the formation of the Lip@$MOMP_2$@AgNCs hydrogel precursor.

2.8. 3D printing of the Lip@$MOMP_2$@AgNCs hydrogel

The Lip@$MOMP_2$@AgNCs hydrogel precursors were loaded into a 5 mL syringe, and the printing model was designed using Biomaker software. The hydrogels were then 3D-printed using a SunP CPD1/Biomaker printer with I2959 as the photoinitiator. Post-printing, the entire structure was cured under 10 mW/cm² UV light at 365 nm for 5 min to ensure structural integrity. The printing parameters included a speed of 10 mm/s, an extrusion rate of 0.9 mm^3/s, and a 25 G needle.

2.9. Antimicrobial evaluation of the Lip@$MOMP_2$@AgNCs hydrogel

The Lip@$MOMP_2$@AgNCs were co-cultured with a concentration of 10^5 CFU/mL of *Escherichia coli* and *C. albicans* for 6 h. Following the co-cultivation period, the microbial cells underwent a washing process with PBS twice and were subsequently immersed in a 2.5% glutaraldehyde solution at 4 °C for 2 h to ensure proper fixation. Post-fixation, the samples were subjected to centrifugation at 3000 rpm for 10 min, followed by two additional washes with PBS. The cells then underwent a dehydration protocol, utilizing a graded series of ethanol solutions—30%, 50%, 70%, and 90%—and culminating in absolute ethanol. After centrifugation to remove the supernatant, the samples were transferred into a mixture of ethanol and tert-butanol in a 1:1 ratio, with subsequent removal of the supernatant. The exchange was completed with two washes using pure tert-butanol. Finally, a 10 μL aliquot of the homogenized bacterial-tert-butanol suspension was carefully deposited onto a silicon wafer and vacuum-dried overnight. After sputter-coating with gold, the samples were subjected to scanning electron microscopy (SEM) analysis.[25]

2.10. *In vitro* antimicrobial testing

In vitro antimicrobial assays were performed against the clinically relevant pathogenic bacteria, *C. albicans* and *E. coli*.[26] The antimicrobial activity of the samples was evaluated by calculating the inhibition rate. Briefly, the aforementioned bacteria were co-cultured at a concentration of 10^7 CFU/mL with various concentrations of AgNCs and Lip@$MOMP_2$@AgNCs in a shaking incubator set at 37 °C and 150 rpm for 6 h. The resulting bacterial suspension was diluted 10^5 times with PBS and evenly spread on Luria–Bertani (LB) agar plates. A blank agar plate was used as a control under the same conditions. After incubation at 37 °C for 12 h, the plates were photographed, and the number of colonies was counted.

2.11. Assessment of cytotoxicity via live/dead cell staining

L929 and HSF cells, at a concentration of 5×10^4 cells/mL, were carefully seeded into 12-well plates and incubated for 24 h at 37 °C under a humidified atmosphere containing 5% CO_2. Subsequently, each well was supplemented with 1 mL of culture medium, which included varying concentrations of AgNCs and composite liposomes, and the plates were returned to the incubator for an additional 24-h period. Following this incubation, 500 μL of a live/

dead cell staining solution was introduced into each well, followed by further incubation for 15 min. The viability of the cells was then meticulously evaluated using an inverted fluorescence microscope, providing insights into the cytotoxic effects of the treatments.

2.12. Hemolysis assay

Initially, 3 mL of human blood was collected and subjected to washing with physiological saline by means of centrifugation at 1500 rpm. The obtained red blood cells were subsequently diluted in physiological saline to prepare a 2% red blood cell suspension. Thereafter, 100 μL of this suspension was combined with 1 mL of varying concentrations of Lip@$MOMP_2$@AgNCs solution. For the negative control group, 100 μL of the red blood cell suspension was mixed with 1 mL of physiological saline, while the positive control group consisted of 100 μL of the suspension added to 1 mL of deionized water. These samples were incubated in a water bath at 37°C for 1 h, followed by centrifugation at 3000 rpm for 15 min. Subsequently, 100 μL of the supernatant was carefully transferred to a 96-well plate, and the optical density (OD) at 540 nm was determined using a microplate reader. The hemolysis rate was then calculated following a specific formula[27,28]:

$$\text{Hemolysis rate}\,(\%) = \frac{OD_{positive} - OD_{negative}}{OD_{sample} - OD_{negative}} \times 100\% \quad (I)$$

2.13. Cell seeding on hydrogel scaffolds

The Lip@$MOMP_2$@AgNCs hydrogel scaffolds were initially submerged in a culture medium and stored at 4 °C overnight to ensure thorough saturation. L929 cells were cultured in RPMI-1640 medium, enriched with 10% fetal bovine serum (FBS), at 37 °C in a 5% CO_2 environment to maintain optimal growth conditions. A cell suspension, containing L929 cells at a concentration of 5×10^6 cells/mL, was meticulously seeded onto the prepared scaffolds. To support cell viability and proliferation, the culture medium was refreshed every two days.

2.14. Study of vaginitis treatment in mice

Seven-week-old female BALB/c mice (20–21 g) were allocated into six distinct groups and allowed a 1-week acclimation period prior to commencing the experiment. The mice were administered subcutaneous injections of estradiol benzoate oil (0.05 mL; 0.2 mg/0.1 mL) on alternate days, totaling three doses. On the sixth day, each mouse was intravaginally inoculated with 5×10^4 spores of *C. albicans* for 3 consecutive days to establish infection. Following this, sterilized samples (physiological saline, Lip@AgNCs, Lip@$MOMP_1$@AgNCs, Lip@$MOMP_2$@AgNCs, and fluconazole) were administered via tail vein injection (100 μL each), and fluorescence imaging was conducted 24 h post-injection to evaluate the biodistribution of Lip@AgNCs and Lip@MOMP@AgNCs across various organs. These injections were repeated at 2-day intervals, for a total of three administrations. In addition, hydrogels containing Lip@AgNCs, Lip@$MOMP_1$@AgNCs, and Lip@$MOMP_2$@AgNCs were applied topically to the vulvar region. A cohort of uninfected mice served as the blank control group ($n = 5$).

Vaginal lavage samples were collected on days 1, 7, 9, 11, 13, 15, 17, 19, and 21. The lavage fluids underwent vortex mixing for 3 min, followed by serial dilution at a 1:1000 ratio. These diluted samples were subsequently plated on agar for further analysis. After a 12-h incubation period, photographs were captured, and colony counts were meticulously conducted to assess fungal growth.

2.15. Statistical analysis

All data were expressed as at least three independent experiments. All the data were analyzed using one-way analysis of variance (ANOVA). Significant differences are indicated at $^*p < 0.05$, $^{**}p < 0.01$, and $^{***}p < 0.001$.

3. Results and discussion

3.1. Preparation and characterization of Lip@$MOMP_2$@AgNCs

In recent years, the escalating prevalence of antibiotic-resistant pathogens has posed profound challenges to public health, necessitating the invention of innovative therapeutic strategies. In response to this medical exigency, we initiated the present study, focusing on the extraction and purification of membrane proteins from J774.A1 macrophage cells, to enhance targeted antibacterial interventions. Specifically, a membrane protein extraction kit was employed to isolate $MOMP_1$ from untreated J774.A1 cells, while $MOMP_2$ was obtained from J774.A1 cells exposed to *C. albicans*. By extracting key receptor proteins, chiefly TLR2 and TLR4, from the membranes of the *Candida*-treated macrophages, we engineered biomimetic vesicles adorned with these proteins (Lip@$MOMP_2$), endowing them with the capability for specific bacterial recognition (Figure 1a). Furthermore, these vesicles were seamlessly integrated with minuscule AgNCs, culminating in Lip@$MOMP_2$@AgNCs (Figure 1b). This avant-garde approach aims to achieve precise targeting and effective treatment of diseases associated with drug-resistant *Candida* species.

SEM images revealed that conventional liposomes (Lip) possess a smooth surface with an average diameter of approximately 151 nm (Figure 1c). In stark contrast, the biomimetic liposomes (Lip@$MOMP_2$) displayed distinct

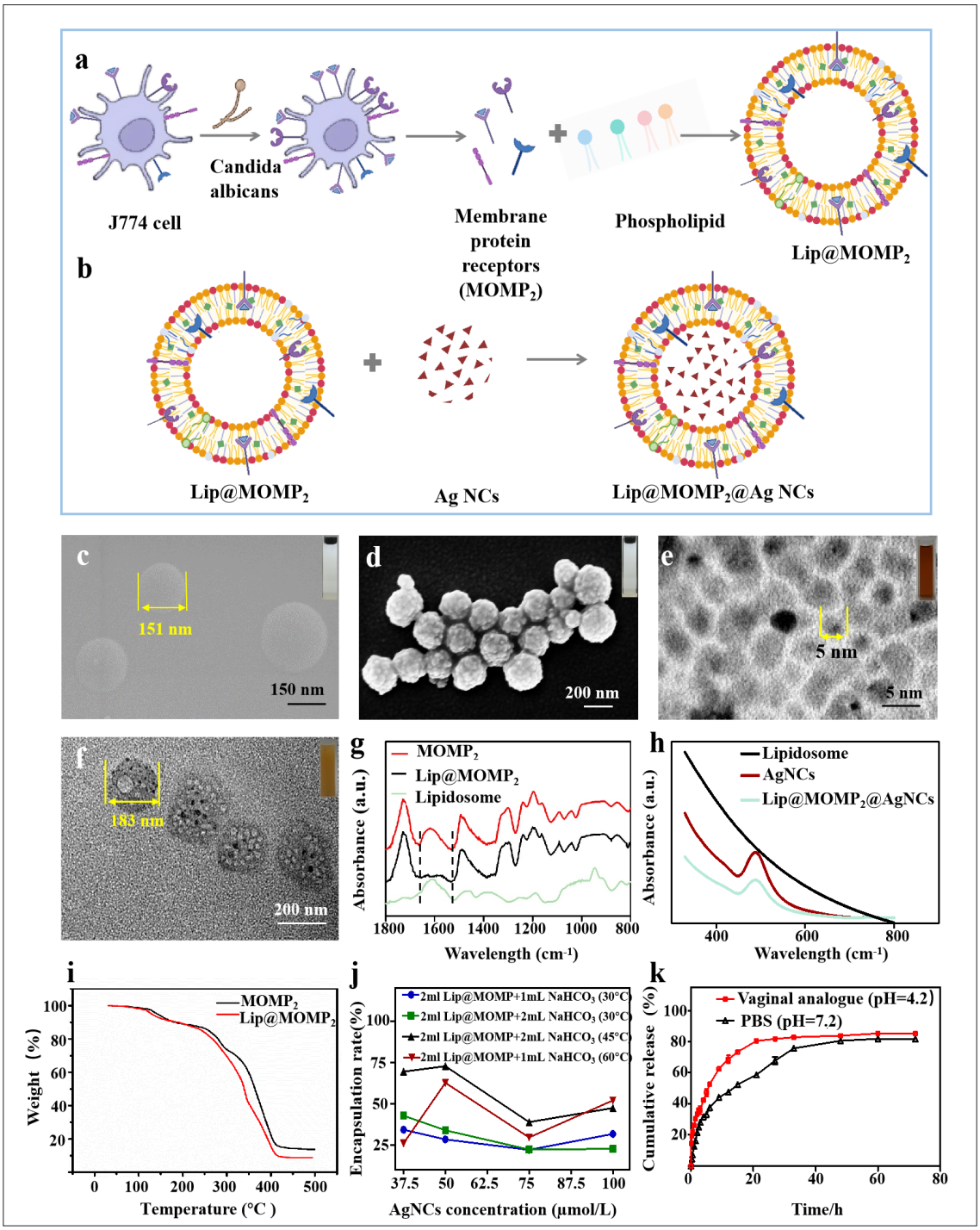

Figure 1. Images of Lip@$MOMP_2$@AgNCs solution. (a) Schematic representation of the synthesis of biomimetic liposomes (Lip@$MOMP_2$). (b) Schematic representation of the synthesis of Lip@$MOMP_2$@AgNCs. (c–e) Scanning electron microscopy (SEM) images of conventional liposomes (Lip; c), biomimetic liposomes (Lip@$MOMP_2$; d), and AgNCs (e). The solutions of Lip, Lip@MOMP2, and AgNCs. (c–e, inset). (f) Transmission electron microscopy (TEM) image of Lip@$MOMP_2$@AgNCs. The solutions of Lip@MOMP2@AgNCs. (f, inset). (g) Fourier-transform infrared spectroscopy (FTIR) spectra of Lip@$MOMP_2$ (red), Lip (black), and $MOMP_2$ (green). The amide region peaks (dashed lines) represent the characteristic absorption region of peptide bonds in proteins. (h) Ultraviolet (UV) spectra of Lip@$MOMP_2$ (black), AgNCs (red), and Lip@$MOMP_2$@AgNCs (green). (i) Thermogravimetric analysis (TGA). (j) Encapsulation efficiency of Lip@$MOMP_2$@AgNCs under varying concentrations of AgNCs, different temperatures, and different amounts of $NaHCO_3$. (k) Cumulative release profiles of Lip@$MOMP_2$@AgNCs in vaginal simulated fluid (pH = 4.2) and phosphate-buffered saline (PBS; pH = 7.2) (n = 3). Scale bars: 150 nm (c); 200 nm (d and f); 5 nm (e). Abbreviation: AgNCs, silver nanoclusters.

surface protrusions (Figure 1d), which we preliminarily identified as the specific receptor proteins ($MOMP_2$) derived from J774.A1 macrophage cell membranes. Dynamic light scattering (DLS) analysis indicated that Lip@$MOMP_2$ predominantly exhibited particle sizes ranging from 100 to 200 nm (Figure S1b, Supporting Information), with a zeta potential of -20.17 mV. According to pertinent studies, negatively charged nanoliposomes within the 100–200 nm size bracket, when delivered via tail vein injection in mice, have around 60% of the injected dose circulating in the bloodstream. This attribute diminishes hepatic accumulation and enhances clearance, thereby significantly mitigating the biotoxicity of Lip@$MOMP_2$. Additionally, the average size of AgNCs was approximately 5 nm (Figures 1e and S1, Supporting Information). Nanoparticles smaller than 6 nm are readily excreted via the renal pathway,[29,30] rendering the synthesized AgNCs a safe antimicrobial candidate for clinical applications. The zeta potential of AgNCs was measured at 3.1 mV (Figure S1, Supporting Information), which facilitates their interaction with the negatively charged Lip@$MOMP_2$. Transmission electron microscopy (TEM) and elemental distribution images of Lip@$MOMP_2$@AgNCs (Figures 1f and S2, Supporting Information) reveal the presence of black dots, confirming the successful encapsulation of AgNCs within Lip@$MOMP_2$.

To further substantiate the successful assembly of Lip and $MOMP_2$, Fourier-transform infrared spectroscopy (FTIR) was employed to analyze Lip, $MOMP_2$, and Lip@$MOMP_2$ (Figure 1g). The amide I (1600–1690 cm^{-1}) and amide II (1480–1575 cm^{-1}) regions correspond to the C=O stretching and N–H bonding of $MOMP_2$, respectively. Notably, distinctive absorption peaks in the amide region were observed in the $MOMP_2$ and Lip@$MOMP_2$ samples, while no such peaks were detected in the Lip group, indicating the successful synthesis of Lip@$MOMP_2$. UV spectroscopy analysis was employed to validate the encapsulation of AgNCs within Lip@$MOMP_2$ (Figure 1h). The results revealed characteristic absorption peaks at 485 nm for both AgNCs and Lip@$MOMP_2$@AgNCs, whereas no absorption peak was present for Lip@$MOMP_2$ at this wavelength, confirming the successful loading of AgNCs into Lip@$MOMP_2$. In summary, Lip@$MOMP_2$@AgNCs have been successfully prepared, and Lip@$MOMP_2$ exhibits favorable thermal stability (Figure 1i).

To refine the encapsulation strategy for Lip@$MOMP_2$, we meticulously explored various parameters, including drug loading temperature, AgNCs concentration, and the amount of 5% $NaHCO_3$. Based on the phase transition temperature of Lip@$MOMP_2$, we established experimental conditions at 30, 45, and 60 °C. Ultimately, it was discerned that at 45 °C, with an AgNCs concentration of 50 μg/mL, in conjunction with 2 mL of biomimetic lipid vesicles and 2 mL of $NaHCO_3$, the encapsulation efficiency attained a pinnacle of 72.76% (Figure 1j). Consequently, the maximal drug loading capacity of Lip@$MOMP_2$@AgNCs was computed to be 11.9%. The drug release profile of Lip@$MOMP_2$@AgNCs is illustrated in Figure 1k. In the vaginal simulation medium, the cumulative release of AgNCs reached 78.4% after 24 h, whereas in PBS at pH 7.2, the cumulative release was 58.2%. After 36 h, the release rates of AgNCs in both media began to stabilize. Overall, Lip@$MOMP_2$@AgNCs exhibited a more rapid release rate of AgNCs in the vaginal simulation medium compared to PBS at pH 7.2, with the release profiles also indicating the sustained-release characteristics of Lip@$MOMP_2$@AgNCs.

3.2. Printability of the Lip@$MOMP_2$@AgNCs hydrogel

In clinical practice, the management of vulvovaginal candidiasis encompasses an initial focus on targeting inflammation at the affected sites, eradicating *C. albicans*, and ensuring optimal ventilation while managing secretions as pivotal elements of supportive therapy. We have equipped Lip@$MOMP_2$@AgNCs with both targeted bacterial recognition capabilities and anti-inflammatory properties. To augment therapeutic efficacy, we engineered a 3D-printed hydrogel scaffold embedded with Lip@$MOMP_2$@AgNCs for localized application in the vulvar region. Through a synergistic approach combining injection and topical application, Lip@$MOMP_2$@AgNCs can precisely identify inflamed sites within the bloodstream. The mesh-like hydrogel scaffold not only conforms intimately to the vulvar anatomical structure, permitting adequate air circulation and facilitating secretion expulsion but also enables the *in situ* release of Lip@$MOMP_2$@AgNCs. Consequently, the integration of injection and topical application of Lip@$MOMP_2$@AgNCs achieves a synergistic enhancement of antimicrobial efficacy.

To facilitate *in situ* release of Lip@$MOMP_2$@AgNCs for antibacterial and anti-inflammatory effects, Lip@$MOMP_2$@AgNCs hydrogels were prepared at varied concentration ratios of HAMA:carbopol (1:2, 3:2, and 5:2). SEM images disclosed the internal porous architectures of these hydrogels, with the 1:2 and 3:2 ratios displaying well-defined network structures (Figure 2a–c). Additionally, the precursor hydrogels of Lip@$MOMP_2$@AgNCs exhibited shear-thinning behavior at elevated shear rates, as demonstrated by the viscosity–shear rate curves. This property underscores their suitability for 3D printing applications under similar shear conditions. The Lip@$MOMP_2$@AgNCs hydrogel exhibits elastic properties, as evidenced by the temporal evolution of the storage modulus

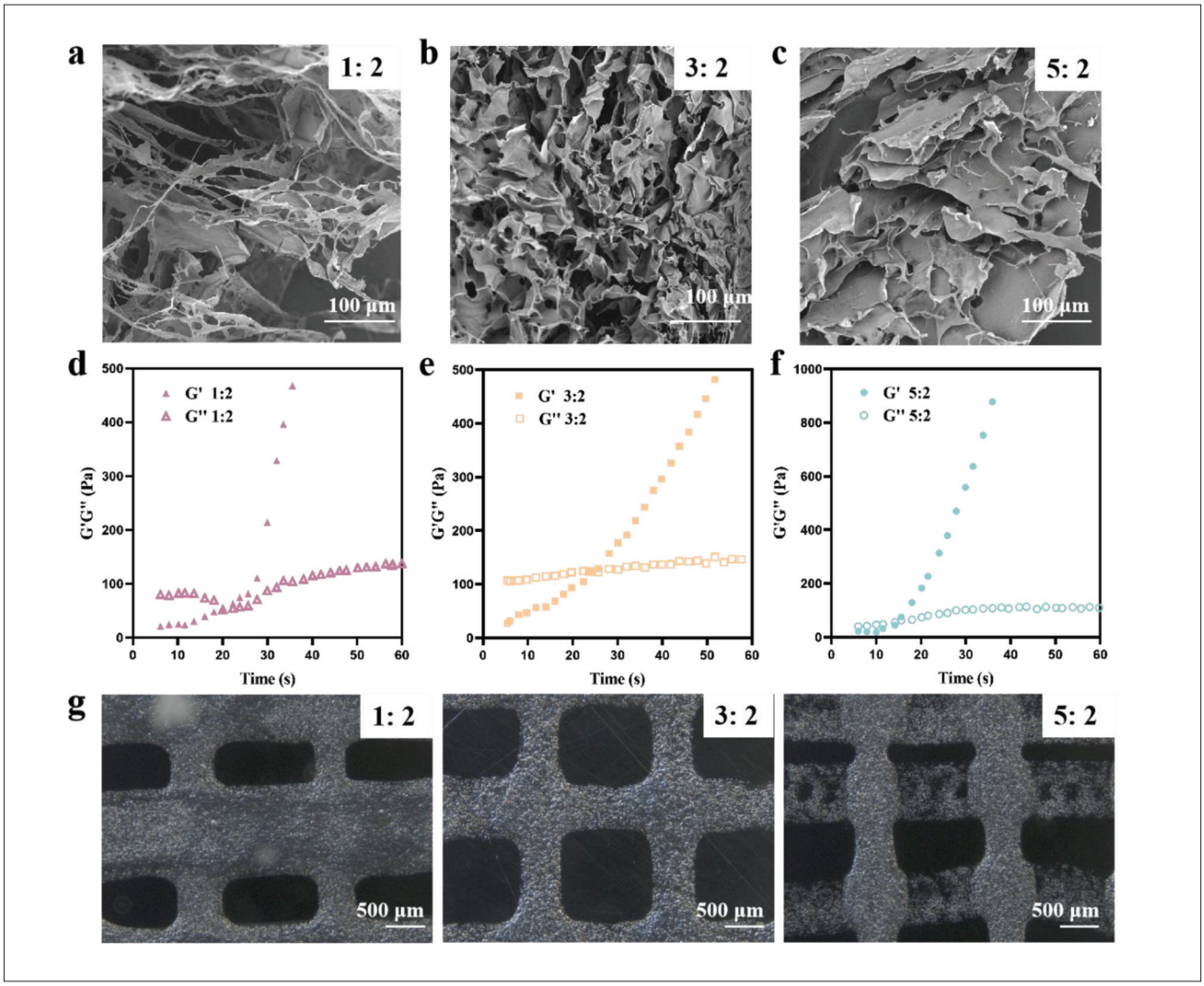

Figure 2. Preparation and characterization of Lip@MOMP$_2$@AgNCs hydrogel. (a–c) Scanning electron microscopy (SEM) images of the cross-section of Lip@MOMP$_2$@AgNCs hydrogel at different ratios of HAMA:Carbopol: 1:2 (a), 3:2 (b), and 5:2 (c). (d–f) Temporal evolution of the storage modulus (*G'*) and loss modulus (*G"*) of hydrogel precursors at different ratios of HAMA:carbopol during ultraviolet (UV) irradiation: 1:2 (d), 3:2 (e), and 5:2 (f). (g) The 3D printing structure of Lip@MOMP$_2$@AgNCs hydrogel at different ratios of HAMA:Carbopol: 1:2, 3:2, and 5:2. Scale bars: 100 μm (a–c); 500 μm (g). Abbreviations: AgNCs, silver nanoclusters; HAMA, hyaluronic acid methacrylate.

(*G'*) and loss modulus (*G"*). As displayed in Figure 2d–f, the storage modulus (*G'*) increases over time and surpasses the loss modulus (*G"*), indicating the transition of the hydrogel into a solid-like state. Moreover, the yield stress results further corroborate the mechanical performance of the hydrogel. The yield stress values for hydrogels with different component ratios (1:2, 3:2, and 5:2) were determined, with calculated values of approximately 71.45, 150.4, and 607.1 Pa, respectively (Figure S3, Supporting Information). These findings demonstrate that the hydrogel's mechanical properties, including elasticity and yield stress, are well-suited to ensuring structural integrity during the 3D printing process. In addition, Figure S4, Supporting Information, demonstrates the swelling and degradation behavior of hydrogels with different ratios of Lip@MOMP$_2$@AgNCs. To evaluate the printability of hydrogels with varying ratios, different formulations were tested. It was determined that the 3:2 ratio of Lip@MOMP$_2$@AgNCs hydrogels yielded the most stable grid structure with the most uniform lines. Consequently, this concentration ratio was selected for subsequent experiments (Figure 2g).

3.3. Biosafety of the Lip@MOMP$_2$@AgNCs hydrogel

To evaluate the biocompatibility of the Lip@MOMP$_2$@AgNCs hydrogel, we conducted co-culture experiments with varying concentrations of AgNCs and Lip@MOMP$_2$@AgNCs in L-929 cells and human umbilical vein endothelial

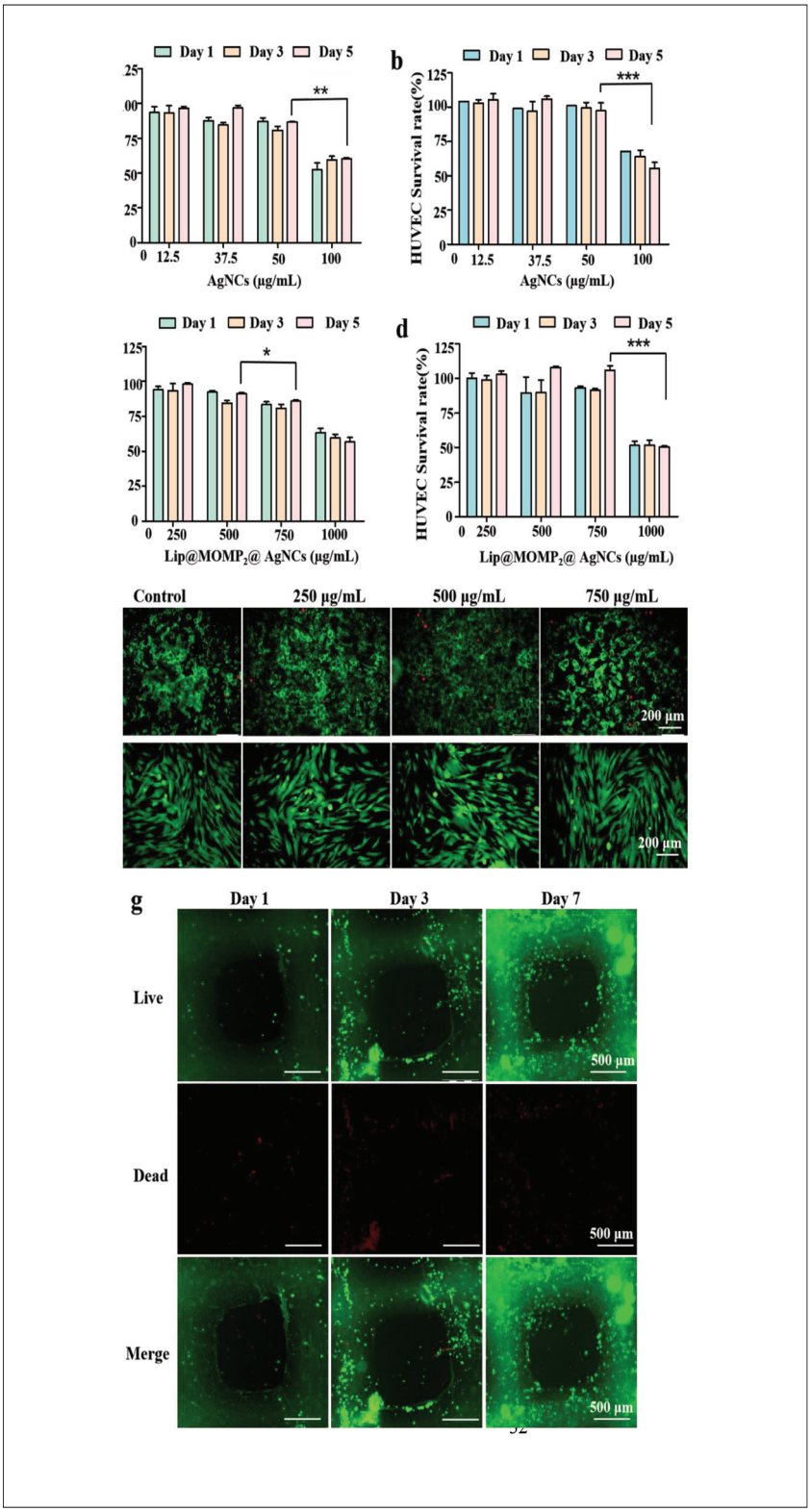

Figure 3. The biocompatibility of the Lip@MOMP$_2$@AgNCs hydrogel. (a–d) Cytotoxicity of different concentrations of AgNCs and Lip@MOMP$_2$@AgNCs hydrogel on L-929 cells (a and c) and human umbilical vein endothelial cells (HUVECs; b and d). *$p < 0.05$; **$p < 0.01$; ***$p < 0.001$. (e and f) Live/dead staining images of L-929 cells (e) and human skin fibroblasts (HSF; f) co-cultured with different concentrations of Lip@MOMP$_2$@AgNCs hydrogel. (g) L-929 cells cultured on Lip@MOMP$_2$@AgNCs hydrogel scaffolds. Scale bars: 200 μm (e and f); 500 μm (g). Abbreviation: AgNCs, silver nanoclusters.

cells (HUVECs) over 1, 3, and 5-day periods. The findings revealed that at concentrations up to 50 μg/mL, cell viability for both L-929 and HUVECs exceeded 85% by day 5 (Figure 3a and b). At a concentration of 750 μg/mL, the viability of L-929 and HUVECs on day 5 was 71.6% and 74.7%, respectively. However, at 500 μg/mL, both cell types exhibited viabilities exceeding 90% (Figure 3c and d). Further corroborating the biocompatibility of the Lip@MOMP$_2$@AgNCs hydrogel, live/dead staining assays conducted on L-929 and human skin fibroblasts (HSFs) aligned with the observed cell viability results (Figure 3e and f). Additionally, L-929 cells cultured on 3D-printed Lip@MOMP$_2$@AgNCs hydrogel scaffolds exhibited robust viability at days 1, 3, and 7, suggesting that the scaffold is conducive to cell growth and demonstrates excellent biocompatibility (Figure 3g).

To further ascertain the safety profile of Lip@MOMP$_2$@AgNCs, hemolysis assays were performed using a 2% red blood cell suspension across various formulations, including AgNPs, AgNCs, Lip@AgNCs, Lip@MOMP$_1$@AgNCs, and Lip@MOMP$_2$@AgNCs. The hemolysis rate for AgNPs was determined to be 12.4%, whereas AgNCs, Lip@AgNCs, and Lip@MOMP$_1$@AgNCs exhibited hemolysis rates below 5%. Notably, the hemolysis rate for Lip@MOMP$_2$@AgNCs was measured at 2.8%, which remains below the 5% threshold, indicating excellent blood compatibility (Figure S5, Supporting Information).

3.4. Antibacterial properties of the Lip@MOMP$_2$@AgNCs hydrogel

Upon confirming the biocompatibility of the AgNCs and Lip@MOMP$_2$@AgNCs hydrogel system, we advanced our investigation to examine its *in vitro* antibacterial efficacy against *E. coli* and drug-resistant *C. albicans*. To elucidate the underlying mechanism, SEM was employed to observe morphological alterations in the microorganisms post-treatment with varying concentrations of Lip@MOMP$_2$@AgNCs hydrogel solutions.

The SEM analysis revealed that both *E. coli* and drug-resistant *C. albicans* experienced notable wrinkling and compromised membrane integrity when exposed to 250 μg/mL Lip@MOMP$_2$@AgNCs hydrogel (Figure 4a and b). At elevated concentrations (500 and 750 μg/mL), complete disruption of the bacterial membranes was observed, leading to cellular shrinkage. Plate count methodology further demonstrated that AgNCs at a concentration of 37.5 μg/mL possessed considerable antibacterial effects against both organisms, with concentrations exceeding 50 μg/mL achieving antibacterial rates surpassing 95% (Figure 4c and d). Remarkably, the antibacterial effect was particularly pronounced at a Lip@MOMP$_2$@AgNCs hydrogel concentration of 500 μg/mL (Figure 4e and f). Given the differential cytotoxicity between the 500 and 750 μg/mL hydrogel concentrations, we ultimately identified 500 μg/mL as the optimal therapeutic concentration for Lip@MOMP$_2$@AgNCs hydrogel.

In exploring the impact of bacteria on immune responses, the pivotal role of Toll-like receptors (TLRs)—pattern recognition receptors located on cell membranes that are integral to the immune system—must be considered. The recognition of microbial pathogens by these receptors is essential for initiating the host's immune response to extracellular pathogens.[31–33] Among the various pattern recognition receptors (PRRs), TLRs were the first to be identified and remain the most extensively studied, known for recognizing a broad spectrum of pathogen-associated molecular patterns (PAMPs).[34] TLR2 and TLR4 stand out as significant receptors, primarily recognizing distinct pathogen components; TLR2 interacts with bacterial peptidoglycan, while TLR4 focuses on bacterial lipopolysaccharides.

In our study, the targeting capability of Lip@MOMP$_2$@AgNCs liposomes was enhanced by incorporating specific receptor proteins, primarily TLR2 and TLR4, extracted from pre-treated macrophage membranes. These receptors are crucial for recognizing bacterial components,[35,36] with TLR2 binding bacterial peptidoglycan and TLR4 recognizing lipopolysaccharides. By incorporating TLR2 and TLR4, Lip@MOMP$_2$@AgNCs liposomes gain enhanced specificity for targeting bacteria.

To assess immune activation and the targeting effect of Lip@MOMP$_2$@AgNCs, we co-cultured J774.A1 cells with *C. albicans* and performed flow cytometry to measure the expression of TLR2, TLR4, and CD45. Notably, after infection, both TLR2 and TLR4 expressions were significantly upregulated. Specifically, the percentage of TLR2-positive cells in the treatment group increased to 94.12%, compared to 84.17% in the control group (Figure S6, Supporting Information). Similarly, TLR4 expression rose to 99.71% in the treatment group, while the control group reported 84.17%. These results suggest that Lip@MOMP$_2$@AgNCs liposomes enhance immune responses by facilitating pathogen recognition through TLR signaling pathways.

In Figure S7, Supporting Information, Western blot analysis confirmed the upregulation of TLR2 and TLR4 in J774.A1 cells co-cultured with *C. albicans*, reinforcing the flow cytometry findings. In contrast, CD45 expression, a marker for leukocytes, displayed a smaller increase (83.22% in the treatment group vs. 81.62% in the control group) (Figure S6, Supporting Information), indicating that the

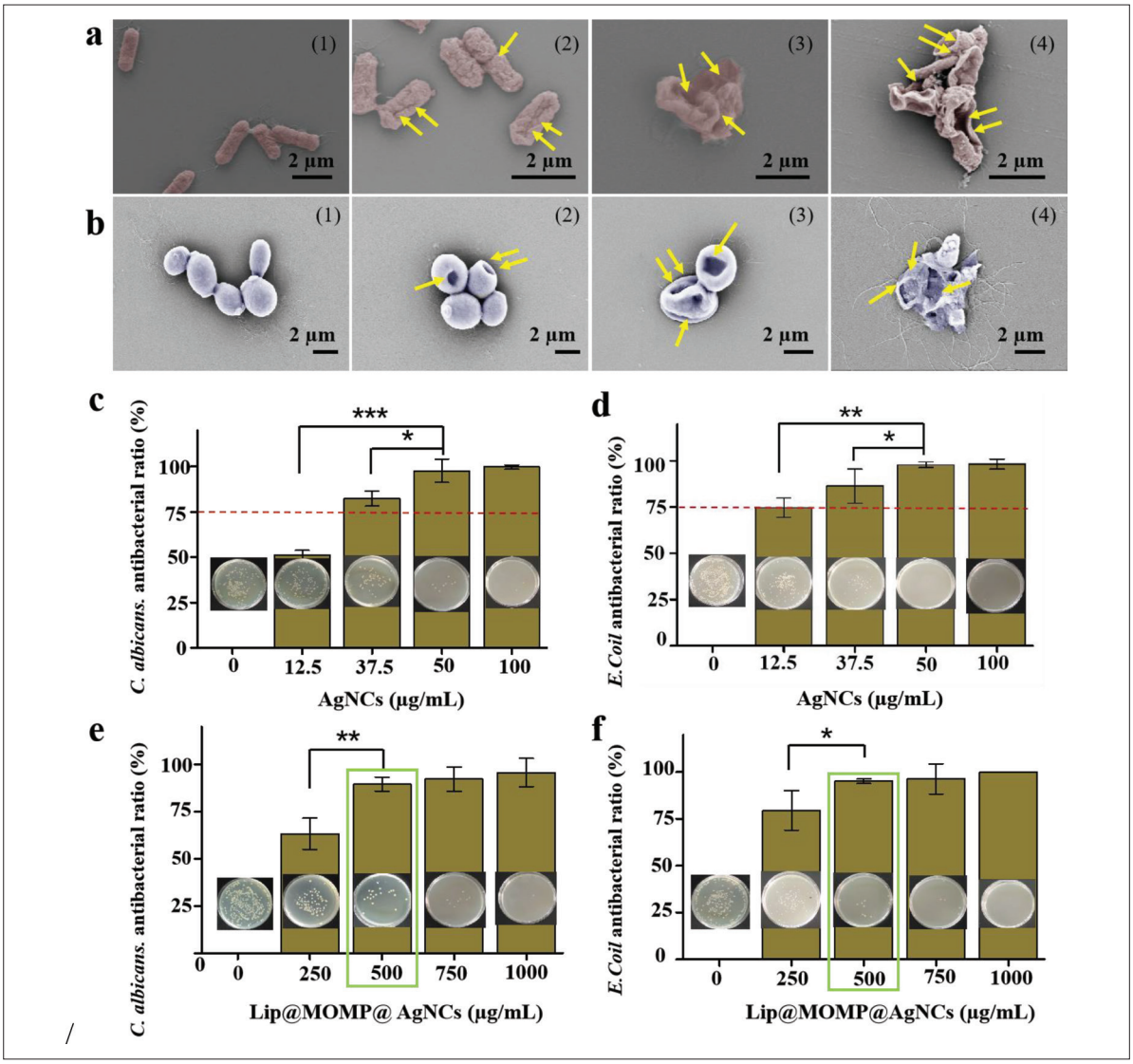

Figure 4. The yellow arrows indicate the locations of bacterial shrinkage. (a and b) Scanning electron microscopy (SEM) images of *Escherichia coli* and *Candida albicans* treated with different concentrations of Lip@MOMP$_2$@AgNCs hydrogel solutions: (1) blank control; (2) 250 μg/mL; (3) 500 μg/mL; and (4) 750 μg/mL. Yellow arrows indicate the locations of bacterial shrinkage. (c and d) Antimicrobial rates of different concentrations of AgNCs against drug-resistant *C. albicans* (c) and *E. coli* (d). The red dashed line represents an antibacterial rate of 75% (e and f). Antimicrobial rates of different concentrations of Lip@MOMP$_2$@AgNCs hydrogel solutions against drug-resistant *C. albicans* (e) and *E. coli* (f). The green boxes denote the Lip@MOMP$_2$@AgNCs hydrogel concentrations selected for subsequent experiments. n =5 (The experiment was conducted with five independent replicates under the same experimental conditions.). *$p < 0.05$; **$p < 0.01$; and ***$p < 0.001$. Scale bars: 2 μm (a and b). Abbreviation: AgNCs, silver nanoclusters.

treatment had a lesser effect on immune cell recruitment. These findings confirm that *C. albicans* infection activates TLR-mediated immune responses and that the incorporation of TLR2 and TLR4 in Lip@MOMP$_2$@AgNCs liposomes can enhance bacterial pathogen recognition. This provides a theoretical foundation for utilizing these liposomes in targeted bacterial therapy,[37–39] with the potential to improve therapeutic outcomes against resistant pathogens.

3.5. Therapeutic efficacy of Lip@MOMP2@AgNCs on *C. albicans* vaginitis *in vivo*

To further substantiate the therapeutic efficacy and targeting precision of the Lip@MOMP$_2$@AgNCs hydrogel system, we developed a murine model of vaginal inflammation for treatment assessment, as depicted in the timeline illustrated in Figure 5a. Histological examination via Hematoxylin/eosin (HE) staining (H&E) staining on day 9 revealed pronounced infiltration of inflammatory cells within the vaginal tissues of the control group, along

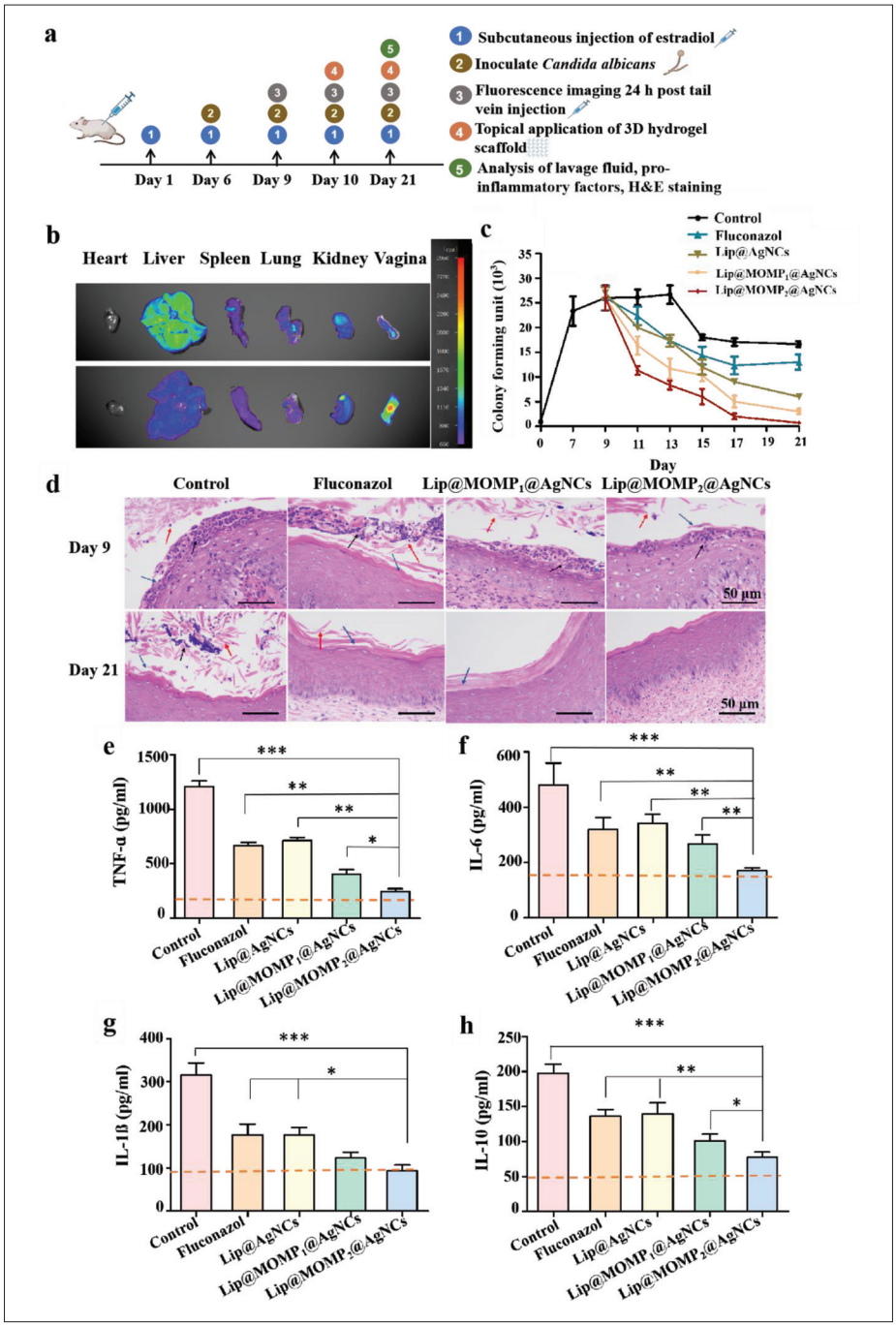

Figure 5. Animal study of Lip@MOMP@AgNCs hydrogel for vginitis treatment. (a) Schematic representation of the establishment and treatment of vaginal inflammation in the mice model. (b) After intravenous injection of Lip@AgNCs or Lip@MOMP@AgNCs, fluorescence imaging displays the distribution of Lip@AgNCs or Lip@MOMP@AgNCs in various organs of the mice 24 h post-injection. (c) Bacterial counts in vaginal lavage fluid collected from the model groups at baseline (day 0) and on days 7, 9, 11, 13, 15, 17, and 21, following a dilution of 10^3 and plating. (d) H&E staining of vaginal tissue from the control group (saline), fluconazole group, Lip@$MOMP_1$@AgNCs hydrogel group, and Lip@$MOMP_2$@AgNCs hydrogel group on days 9 and 21 (post-treatment). Black arrows: abundant neutrophils; red arrows: shed vaginal epithelial cells; blue arrows: damaged vaginal epithelial cells. (e–h) Expression levels of TNF-α, IL-6, IL-1β, and IL-10 in vaginal tissue from the control group, fluconazole group, Lip@AgNCs group, Lip@$MOMP_1$@AgNCs group, and Lip@$MOMP_2$@AgNCs group ($n = 3$; $^*p < 0.05$; $^{**}p < 0.01$; $^{***}p < 0.001$). The dashed orange line represents the expression levels of pro-inflammatory factors in the blood of normal mice. Abbreviations: AgNCs, silver nanoclusters; H&E, hematoxylin and eosin.

with evident cellular damage. This was accompanied by a significant upregulation of pro-inflammatory cytokines TNF-α, IL-6, IL-1β, and IL-10 in the bloodstream, highlighting a marked disparity in pro-inflammatory factor expression between the model and normal mice. This confirms the successful establishment of a mouse model of drug-resistant *C. albicans* vaginitis, providing a robust platform for further investigations.

To verify the targeting capacity of the $MOMP_2$ protein-decorated liposomes, we administered either Lip@AgNCs or Lip@$MOMP_2$@AgNCs via tail vein injection on Day 9. Fluorescent imaging performed 24 h post-injection demonstrated that Lip@AgNCs primarily accumulated in the hepatic region, whereas Lip@$MOMP_2$@AgNCs predominantly localized within the vaginal tissues (Figure 5b). This finding corroborates the targeting capability of the $MOMP_2$ protein, informing the design of subsequent therapeutic strategies.

To amplify the therapeutic effect, a 3D-printed hydrogel mesh scaffold containing Lip@$MOMP_2$@AgNCs was applied locally to the vulvar region, facilitating the *in situ* release of the therapeutic agent. This strategy, combining systemic injection with topical application, achieved a synergistic antimicrobial effect. Bacterial load assessments in the vaginal wash of the inflammatory model mice on Day 9 revealed counts of 2.5×10^4, compared to only 8×10^2 in normal mice, indicating a substantial increase. This prompted an examination of bacterial count changes in vaginal tissues (Figure 5c). The antibacterial efficacy of Lip@$MOMP_2$@AgNCs hydrogel was recorded as 64.1%, 78.3%, and 92.1% on days 11, 15, and 21, respectively, compared to 21.7%, 59.8%, and 63.9% for Lip@AgNCs, and 41.7%, 56.5%, and 78.3% for Lip@MOMP1@AgNCs. In contrast, fluconazole only achieved a 44.3% antibacterial rate by Day 21, markedly lower than that of the Lip@$MOMP_2$@AgNCs group.

As depicted in Figures 5d and S8, Supporting Information, by Day 21 of treatment, the fluconazole group still exhibited significant inflammatory cell presence and epithelial damage in vaginal tissues. The Lip@$MOMP_1$@AgNCs hydrogel group exhibited only slight epithelial damage, while the Lip@$MOMP_2$@AgNCs hydrogel group exhibited no substantial tissue damage, underscoring the differential efficacy of the treatments. Moreover, histopathological analysis revealed no significant histological alterations in major organs (heart, liver, spleen, lungs, and kidneys) between the Lip@$MOMP_2$@AgNCs group and the control group of normal mice (Figure S9, **Supporting Information**), indicating low systemic toxicity and supporting the potential for clinical application.

Data in Figures 5e–h demonstrate that fluconazole modestly reduced TNF-α, IL-6, IL-1β, and IL-10 levels by 40.2%, 63.6%, 49.4%, and 34.7%, respectively. The Lip@AgNCs group exhibited reductions of 38.9%, 56.1%, 46.3%, and 32.8%. Lip@$MOMP_1$@AgNCs treatment decreased inflammatory secretion by 61.2%, 52.9%, 59.4%, and 34.7%. In comparison, Lip@$MOMP_2$@AgNCs achieved substantial downregulation of TNF-α, IL-6, IL-1β, and IL-10 by 72%, 61.3%, 64.7%, and 62.5%, respectively. While the fluconazole group displayed some downregulation of inflammatory markers, it was significantly less pronounced than in the Lip@$MOMP_2$@AgNCs group. Post-treatment, pro-inflammatory factor expression levels in the Lip@$MOMP_2$@AgNCs hydrogel group approached normalcy. In summary, the therapeutic efficacy of Lip@$MOMP_2$@AgNCs against drug-resistant *C. albicans* vaginitis surpassed that of both Lip@$MOMP_1$@AgNCs and fluconazole, with the effectiveness hierarchy being Lip@$MOMP_2$@AgNCs > Lip@$MOMP_1$@AgNCs > fluconazole.

4. Conclusion

In this study, we successfully engineered a sophisticated nanoparticle drug delivery system designed to enhance the antibacterial efficacy against resistant *C. albicans* by ingeniously integrating specific receptor proteins derived from macrophage membranes with diminutive AgNCs. The resultant composite biomimetic liposome, Lip@$MOMP_2$@AgNCs, exhibits an impressive capacity to accurately target infection sites via intravenous administration, demonstrating precise bacterial recognition and specificity. This is coupled with excellent biocompatibility and therapeutic efficacy.

Furthermore, the strategic incorporation of a 3D-printed hydrogel scaffold embedded with Lip@$MOMP_2$@AgNCs allows for sustained and localized drug release, thereby amplifying the antibacterial effect and concurrently minimizing potential adverse side effects. The findings indicate that Lip@$MOMP_2$@AgNCs offers substantial advantages in treating drug-resistant *C. albicans* vaginitis, evidenced by superior antibacterial rates and more effective modulation of inflammatory markers compared to conventional fluconazole therapy. This innovative therapeutic strategy provides a highly effective solution for managing resistant bacterial infections and offers novel insights for optimizing clinical treatment protocols.

Overall, our research presents a groundbreaking approach for the treatment of resistant *C. albicans* vaginitis and paves the way for potential future directions in antibacterial drug development. This work showcases

promising clinical application prospects and holds significant scientific value.

Acknowledgments

None.

Funding

This work was financially supported by the National Key Research and Development Project (2022YFC2403100; 2022YFC2403104), the National Natural Science Foundation of China (81772069, 81801911), and the Medical and Health Science and Technology Project of the Zhejiang Province (2020KY786).

Conflict of interest

The authors declare they have no competing interests.

Author contributions

Conceptualization: Wenyan Wang, Lina Dong, Bixing Fang
Data curation: Wenyan Wang, Lina Dong
Formal analysis: Bixing Fang, Aobuliaximu Yakupu
Funding acquisition: Xingang Wang, Chunmao Han
Investigation: Meixuan Liu, Miao Pan, Xiaoqi Li
Project administration: Xingang Wang
Supervision: Xingang Wang, Qiong Li
Writing – original draft: Wenyan Wang, Lina Dong
Writing – review & editing: Lina Dong, Xingang Wang

Ethics approval and consent to participate

All procedures were performed with the approval of the Animal Ethics Committee of Tsinghua Shenzhen International Graduate School, Tsinghua University (202246).

Consent for publication

Not applicable.

Availability of data

Data is available from the corresponding author upon reasonable request.

References

1. Rodero CF, Fioramonti Calixto GM, Dos Santos KC, et al. Curcumin-loaded liquid crystalline systems for controlled drug release and improved treatment of vulvovaginal candidiasis. *Mol Pharm*. 2018;15(10):4491-4504. doi: 10.1021/acs.molpharmaceut.8b00507
2. Sheary B, Dayan L. Recurrent vulvovaginal candidiasis. *Austral Fam Phys*. 2005;34(3):147-150. doi: 10.1016/j.ajog.2015.06.067
3. Story K, Sobel R. Fluconazole prophylaxis in prevention of symptomatic *candida* vaginitis. *Curr Infect Dis Rep.* 2020;22(1):2. doi: 10.1007/s11908-020-0712-7
4. Tietz H-J. Fluconazole for recurrent vulvovaginal candidiasis. *Medizinische Monatsschrift fur Pharmazeuten* 2009;32(6):227. doi: 10.1055/s-0029-155292
5. Khan Z, Ahmad S, Asadzadeh M. A pilot study showing fluconazole and flucytosine activities against candida glabrata are affected by low ph: implications for the treatment of recurrent vulvovaginal candidiasis. *Clin Exp Obstet Gynecol.* 2024;51(2):39. doi: 10.31083/j.ceog5102039
6. Ying Y, Zhang J, Huang SB, et al. Fluconazole susceptibility of 3,056 clinical isolates of candida species from 2005 to 2009 in a tertiary-care hospital. *Indian J Med Microbiol.* 2015;33(3):413-415. doi: 10.4103/0255-0857.158569
7. Martins Maciel AA, Cunha FA, Freire TM, et al. Development and evaluation of an anti-candida cream based on silver nanoparticles, *3 Biotech.* 2023;13(11):352. doi: 10.1007/s13205-023-03776-9
8. Zhang C, Yang X, Yu L, et al. Electrospun polyasparthydrazide nanofibrous hydrogel loading with in-situ synthesized silver nanoparticles for full-thickness skin wound healing application. *Mater Design.* 2024;239:112818. doi: 10.1016/j.matdes.2024.112818
9. Zhang H, Zhang Y, Li Y, et al. A novel silver nanoparticles-decorated metal-organic framework with rapid and sustained antimicrobial activity against drug-resistant *candida albicans* through synergistic chemodynamic and sonodynamic therapy. *Adv Ther.* 2023;6(8):2300074. doi: 10.1002/adtp.202300074
10. Akter M, Sikder MT, Rahman MM, et al. A systematic review on silver nanoparticles-induced cytotoxicity: physicochemical properties and perspectives. *J Adv Res.* 2017;9:1-16. doi: 10.1016/j.jare.2017.10.008
11. Nasim I, Kumar SR, Vishnupriya V, et al. Cytotoxicity and anti-microbial analysis of silver and graphene oxide bio nanoparticles. *Bioinformation*. 2020;16(11):831-836. doi: 10.1016/j.jare.2017.10.008
12. Wolff N, Bialas N, Loza K, et al. Increased cytotoxicity of bimetallic ultrasmall silver-platinum nanoparticles (2 nm) on cells and bacteria in comparison to silver nanoparticles of the same size. *Materials (Basel)*. 2024;17(15):3702. doi: 10.3390/ma17153702
13. Yuan X, Setyawati MI, Tan AS, et al. Highly luminescent silver nanoclusters with tunable emissions: cyclic reduction-decomposition synthesis and antimicrobial properties, *NPG Asia Mater.* 2013;5:e39. doi: 1038/am.2013.3

14. Ai F, Liu T, Liu Y, et al. A 3d printed wound cooling system incorporated with injectable, adsorbable, swellable and broad spectrum antibacterial scaffolds for rapid hematischesis processing. *J Mater Chem B*. 2018;6(37):5940-5948. doi: 10.1039/c8tb01625a

15. Wang C, Wang Y, Zhang L, et al. Pretreated macrophage-membrane-coated gold nanocages for precise drug delivery for treatment of bacterial infections. *Adv Mater.* 2018;30(46):e1804023. doi: 10.1002/adma.201804023

16. Taylor PR, Martinez-Pomares L, Stacey M, Lin HH, Brown GD, Gordon S. Macrophage receptors and immune recognition. *Annu Rev Immunol*. 2005;23:901-944. doi: 10.1146/annurev.immunol.23.021704.115816

17. Yu L, Pan J, Du L, et al. Novel roles of tlr2and tlr4in innate immunity against virus infections. *Chin J Virol.* 2018;34(4):570-578. doi: 10.1016/j.bjid.2015.10.011

18. Gao Q, Lee J-S, Kim BS, et al. Three-dimensional printing of smart constructs using stimuli-responsive biomaterials: a future direction of precision medicine. *Int J Bioprint.* 2023;9(1):230-257. doi: 10.18063/ijb.v9i1.638

19. Li Z, Zheng A, Mao Z, et al. Silk fibroin-gelatin photo-crosslinked 3D-bioprinted hydrogel with MOF-methylene blue nanoparticles for infected wound healing. *Int J Bioprint.* 2023;9(5):459-473. doi: 10.18063/ijb.773

20. Chen H, Zhang X, Shang L, et al. Programmable anisotropic hydrogels with localized photothermal/magnetic responsive properties. *Adv Sci*. 2022;9(26): 2202173-2202182. doi: 10.1002/advs.202202173

21. Chen XB, Anvari-Yazdi AF, Duan X, et al. Biomaterials/bioinks and extrusion bioprinting. *Bioact Mater.* 2023;28:511-536. doi: 10.1016/j.bioactmat.2023.06.006

22. Ng WL, Shkolnikov V. Jetting-based bioprinting: process, dispense physics, and applications. *Bio-Design Manuf.* 2024;7(2):771-799. doi: 10.1007/s42242-024-00285-3

23. Li Y, Zhang X, Zhang X, et al. Recent progress of the vat photopolymerization technique in tissue engineering: a brief review of mechanisms, methods, materials, and applications. *Polymers*. 2023;15(19):3940-3975. doi: 10.3390/polym15193940

24. Guo Z, Mi S, Sun W. A facile strategy for preparing tough, self-healing double-network hyaluronic acid hydrogels inspired by mussel cuticles. *Macromol Mater Eng.* 2019;304(4):1800715. doi: 10.1002/mame.201800715

25. Ouyang J, Liu R-Y, Chen W, et al. A black phosphorus based synergistic antibacterial platform against drug resistant bacteria. *J Mater Chem B*. 2018;6(39):6302-6310. doi: 10.1039/c8tb01669k

26. Munshi R, Talele G, Shah R. *In-vitro* evaluation of antimicrobial activities of *Escherichia coli*, *Klebsiella pneumoniae*, *Salmonella typhi*, *Neisseria gonorrhoeae*, and *Candida albicans* nosodes. *Homeopathy*. 2022;111(01):42-48. doi: 10.1055/s-0041-1727149

27. Henkelman S, Rakhorst G, Blanton J, et al. Standardization of incubation conditions for hemolysis testing of biomaterials. *Mater Sci Eng C*. 2009;29(5):1650-1654. doi: 10.1016/j.msec.2009.01.002

28. Teng Z, Wang S, Su X, et al. Facile synthesis of yolk-shell structured inorganic-organic hybrid spheres with ordered radial mesochannels. *Adv Mater.* 2014;26(22):3741-3747. doi: 10.1002/adma.201400136

29. Liang G, Jin X, Zhang S, et al. RGD peptide-modified fluorescent gold nanoclusters as highly efficient tumor-targeted radiotherapy sensitizers. *Biomaterials*. 2017;144:95-104. doi: 10.1016/j.biomaterials.2017.08.017

30. Qi Y, Xu M, Lu H, et al. Hepatic biotransformation of renal clearable gold nanoparticles for noninvasive detection of liver glutathione level via urinalysis. *Angew Chem Int Ed Engl*. 2024;63(36):e202409477. doi: 10.1002/anie.202409477

31. Yin W, Yu J, Lv F, et al. Functionalized nano-mos with peroxidase catalytic and near-infrared photothermal activities for safe and synergetic wound antibacterial applications. *ACS Nano*. 2016;10(12):11000-11011. doi: 10.1021/acsnano.6b05810

32. Netea MG, Van Der Meer JWM, Kullberg BJ. Toll-like receptors as an escape mechanism from the host defense. *Trends Microbiol.* 2004;12(11):484-488. doi: 10.1016/j.tim.2004.09.004

33. Sasai M, Yamamoto M. Pathogen recognition receptors: ligands and signaling pathways by toll-like receptors. *Int Rev Immunol.* 2013;32(2):116-133. doi: 10.3109/08830185.2013.774391

34. Quesniaux V, Fremond C, Jacobs M, et al. Toll-like receptor pathways in the immune responses to mycobacteria. *Microbes Infect*. 2004;6(10):946-959. doi: 10.1016/j.micinf.2004.04.016

35. Simpson ME, Petri WA, Jr. TLR2 as a therapeutic target in bacterial infection. *Trends Mol Med*. 2020;26(8):715-717. doi: 10.1016/j.molmed.2020.05.006

36. Udgata A, Dolasia K, Ghosh S, Mukhopadhyay S. Dribbling through the host defence: targeting the TLRs by pathogens. *Crit Rev Microbiol*. 2019;45(3):354-368. doi: 10.1080/1040841X.2019.1608904

37. Choudhury QJ, Ambati S, Link CD, Lin X, Lewis ZA, Meagher RB. Dectin-3-targeted antifungal liposomes efficiently bind and kill diverse fungal pathogens. *Mol Microbiol*. 2023;120(5):723-739. doi: 10.1111/mmi.15174

38. Jani K, Mehta S, Patel R, Prajapati B, Patel G. Focused insights into liposomal nanotherapeutics for antimicrobial treatment. *Curr Med Chem*. 2024.
doi: 10.2174/0109298673322058241003073312

39. Singh I, Kumar S, Singh S, Wani MY. Overcoming resistance: chitosan-modified liposomes as targeted drug carriers in the fight against multidrug resistant bacteria-a review. *Int J Biol Macromol*. 2024;278(Pt 4):135022.
doi: 10.1016/j.ijbiomac.2024.135022